JGR Space Physics

RESEARCH ARTICLE
10.1029/2021JA029992

**Key Points:**

- For the first time, we present two-dimensional images of 135.6 nm nightglow from a low-latitude plasma blob
- Evolution history of the blob is gleaned from time series of 135.6 nm nightglow and total electron content images on a continental-scale (>2,000 km)
- Characteristics of this blob event conform to neither medium-scale traveling ionospheric disturbance nor monotonically decaying near-sunset equatorial ionization anomaly crests

**Supporting Information:**

Supporting Information may be found in the online version of this article.

**Correspondence to:**

J. Park,
pj@kasi.re.kr

**Citation:**

Park, J., Huang, C.-S., Eastes, R. W., & Coster, A. J. (2022). Temporal evolution of low-latitude plasma blobs identified from multiple measurements: ICON, GOLD, and Madrigal TEC. *Journal of Geophysical Research: Space Physics*, *127*, e2021JA029992. https://doi.org/10.1029/2021JA029992

Received 29 SEP 2021
Accepted 25 FEB 2022

**Author Contributions:**

**Conceptualization:** Jaeheung Park
**Data curation:** Richard W. Eastes, Anthea J. Coster
**Investigation:** Chao-Song Huang
**Methodology:** Chao-Song Huang
**Software:** Jaeheung Park
**Writing – original draft:** Jaeheung Park
**Writing – review & editing:** Chao-Song Huang, Richard W. Eastes



# Temporal Evolution of Low-Latitude Plasma Blobs Identified From Multiple Measurements: ICON, GOLD, and Madrigal TEC

**Jaeheung Park[1,2], Chao-Song Huang[3], Richard W. Eastes[4], and Anthea J. Coster[5]**

[1]Space Science Division, Korea Astronomy and Space Science Institute, Daejeon, South Korea, [2]Department of Astronomy and Space Science, Korea University of Science and Technology, Daejeon, South Korea, [3]Air Force Research Laboratory, Space Vehicles Directorate, Kirtland AFB, Albuquerque, NM, USA, [4]Laboratory for Atmospheric and Space Physics, University of Colorado Boulder, Boulder, CO, USA, [5]Haystack Observatory, Massachusetts Institute of Technology, Westford, MA, USA

**Abstract** Low-latitude plasma blobs have been studied since their first being reported in 1986. However, investigations on temporal evolution of a blob or on continental scale (>2,000 km) ionospheric contexts around it are relatively rare. Overcoming these limitations can help elucidate the blob generation mechanisms. On 21 January 2021, the Ionospheric Connection Explorer satellite encountered a typical low-latitude blob near the northeastern coast of South America. The event was collocated with a local enhancement in 135.6 nm nightglow at the poleward edge of an equatorial plasma bubble (EPB), as observed by the Global-scale Observations of the Limb and Disk (GOLD) imager. Total electron content maps from the Global Navigation Satellite System confirm the GOLD observations. Unlike typical medium-scale traveling ionospheric disturbances (MSTIDs), the blob had neither well-organized wavefronts nor moved in the southwest direction. Neither was the blob a monotonically decaying equatorial ionization anomaly crest past sunset. Rather, the blob varied following latitudinal expansion/contraction of EPBs at similar magnetic longitudes. The observational results support that mechanisms other than MSTIDs, such as EPBs, can also contribute to blob generation.

**Plain Language Summary** In the nightside low-latitude ionospheric F-layer, localized enhancements of plasma density are occasionally identified, which were named by the ionospheric community as low-latitude plasma blobs. The phenomenon has been extensively investigated since the first report in 1986. However, there have been few studies on temporal evolution of a specific blob or on a continental scale (>2,000 km) ionospheric context around it. In this study, we present two-dimensional images of 135.6 nm nightglow and total electron content, both of which represent ionospheric density, over a wide area (>2,000 km) surrounding a typical blob encountered by the NASA-ICON satellite. According to the time series of the images, the blob is a part of the enhanced plasma contents sitting on the poleward border of an equatorial plasma bubble (EPB). The blob neither exhibited well aligned wavefronts nor propagated equatorward, unlike generic properties of medium-scale traveling ionospheric disturbances (MSTIDs). The results imply that this event did not originate from MSTIDs, but other generation mechanism such as EPBs should be invoked.

## 1. Introduction

In the low-/mid-latitude ionospheric community, "plasma blob" generally signifies localized regions of plasma density enhancement in the tropical ionospheric F-region. Since they were first reported by Oya et al. (1986) and Watanabe and Oya (1986), there have been many observational studies: using in situ plasma density (e.g., Choi et al., 2012; Haaser et al., 2012; Le et al., 2003), ground-based radio images (Yokoyama et al., 2007), all-sky camera (e.g., Martinis et al., 2009), single Global Positioning System receiver (Chen et al., 2008; Wang et al., 2015), and in situ magnetic field observations (e.g., Park et al., 2015). However, theoretical analyses (e.g., Krall et al., 2010, 2009) based on rigorous computer simulations have been relatively rare. V. P. Kim and Hegai (2016) recently reviewed such events.

To date, two blob generation mechanisms have been examined. One mechanism suggests that blobs are related to the dynamics of equatorial plasma bubbles (EPBs), which can again sub-categorized into two cases. According to Le et al. (2003), the locally enhanced polarization E-field inside EPBs is mapped poleward along geomagnetic field lines down to the crests of the equatorial ionization anomaly (EIA). Even if EPBs have a finite latitudinal

extent, the E-field therein does not, which can locally uplift high-density plasma of the EIA peaks to form blobs. On the other hand, simulations of Krall et al. (2010, 2009) showed that meridional wind can change the distribution of plasma density within an EPB flux tube and result in the formation of plasma density enhancement (blob) at one end of the flux tube.

Huang et al. (2014, Figure 8) similarly suggested that updraft of EPBs can deform iso-density contours upwards and later push the high-density region polewards/downwards along magnetic field lines, which leads to blobs. Such deformation of iso-density contours above EPBs can also be seen in EPB simulations in Yokoyama et al. (2015, Figures 2 and 3) although those authors did not explicitly discuss it.

Another mechanism suggests that EPBs need not be associated with blob generation. Choi et al. (2012), Haaser et al. (2012), and Kil et al. (2011) demonstrated that plasma blobs may be encountered in the absence of EPBs. Kil et al. (2019) also presented several examples of topside blobs collocated with medium-scale traveling ionospheric disturbances (MSTIDs) at mid-latitudes, and suggested a close connection between the two phenomena.

Most previous studies of plasma blobs are based on in situ plasma data from low-Earth-orbit (LEO) satellites (e.g., Choi et al., 2012; Huang et al., 2014; Le et al., 2003), and revealed little about the two- or three-dimensional configuration of the structures or their temporal evolution. Thus, the mechanisms responsible for blob formation remain uncertain.

Only a few articles have addressed the two-dimensional structures of blobs and their temporal evolution, but each study had its own limitations. Ground-based 630.0 nm imaging (e.g., Martinis et al., 2009; Pimenta et al., 2004) has a limited field-of-view (FOV) radius of about 1,000 km: in contrast, EPBs can extend to $\pm 20°$ in latitude (e.g., Kil et al., 2004). Also, the 630.0 nm images cannot be free from the ambiguity between the neutral and plasma density (e.g., Makela & Kelley, 2003, Equation 1). Hence, it is not yet decisive whether the localized enhancements in 630.0 nm images reflect actual plasma blobs or just a swell of neutral density. Kil et al. (2019) presented total electron content (TEC) maps of a few blob events and suggested that the blobs originated from MSTIDs. The images were confined to a small region at mid-latitudes (i.e., only above Japan). Until now, no such two-dimensional TEC maps have been reported for low-latitude (e.g., $<20°$ in magnetic latitudes) blobs.

It is clear that more insight into blob formation mechanisms will be aided by examination of the temporal evolution and the two-dimensional context using a time series of images (a) with continental scales (>2,000 km), (b) at low-to-middle latitudes, and (c) with multicolor nightglow or TEC data. This is the motivation of this case study, where we report on a low-latitude plasma blob simultaneously observed by multiple space-based and ground-based instruments. Combining LEO satellite data with continental-scale maps of TEC and 135.6 nm Far-Ultra-Violet (FUV) emissions, we investigate ionospheric contexts around the blob and their temporal evolution to deduce possible generation mechanisms. In the following, Section 2 will give a brief overview of the instruments and data sets used. Section 3 presents observation data, which will be discussed in detail and compared with previous studies in Section 4. Finally, main conclusions will be drawn in Section 5.

## 2. Instruments and Data Set

The Ionospheric Connection Explorer (ICON; see Immel et al., 2018) is an LEO satellite launched in October 2019. The orbit has an altitude of about 600 km and inclination angle of 27°. The spacecraft carries a suite of ionospheric/thermospheric remote sensing instruments, including a Michelson Interferometer for Global High-Resolution Thermospheric Imaging, Extreme Ultra-Violet instrument, and FUV instrument, all of which provide key ionospheric and thermospheric parameters in the northern limb. An Ion Velocity Meter (IVM) measures the ionospheric plasma properties at the spacecraft location. The ICON/IVM measures ion density, velocity, composition, and temperature at a data rate of 1 Hz (Heelis et al., 2017). The total plasma density will be used in this study as a prime detector of blobs. All the ICON data are available at the public repository (ftp://icon-science.ssl.berkeley.edu/pub/LEVEL.2/).

The Global-scale Observations of the Limb and Disk (GOLD) mission has an FUV imager onboard a communication satellite at a geosynchronous (GEO) orbit, SES-14. It was launched in January 2018 into the geographic longitude (GLON) of 47.5°W and has been observing the ionosphere and thermosphere in the American and Atlantic region in the wavelength range between 134 and 162 nm (Eastes et al., 2020). There are 4 primary operation modes, which take turns mainly depending on the local time (LT): dayside disk, limb, stellar occultation,

and nightside disk. In this study, we use the nightside disk data (product identifier "NI1"), which can provide time series of two-dimensional images of 135.6 nm nightglow that represents oxygen ion content (approximately equal to ionospheric density): for example, see Rajesh et al. (2011). The nightside disk images are given every 15 min from 20:10 in Universal Time (UT) until 00:25 UT next day when the mode stops to avoid direct sunlight incidence. As the GOLD FOV changes positions with UT (e.g., in Africa at 20:10 UT and in South America at 00:25 UT), only the part of the time series relevant to the American-Atlantic region will be used in this study.

The Coupling, Energetics, and Dynamics of Atmospheric Regions (CEDAR) Madrigal database provide global TEC maps with a spatial resolution of 1°×1° in geographic latitude (GLAT) and GLON every 5 min. The data are obtained by the ground-based observations of the Global Navigation Satellite System (GNSS) signals and freely available at http://cedar.openmadrigal.org/. Detailed processing methods are given in Rideout and Coster (2006) and Vierinen et al. (2016). As most of the TEC data sources are located above landmasses, the CEDAR Madrigal TEC maps generally have large data gaps above oceans. Also, even the data above landmasses can contain gaps depending on the visibility of GNSS satellites. In this study, we combine two consecutive 5 min TEC maps into one 10 min image to alleviate the data gaps.

The magnetic latitude (MLAT) and longitude (MLON) can be useful in addressing conjugacy between different phenomena at different locations. Throughout this study, we use the quasi-dipole coordinate system as defined by Laundal and Richmond (2017) at the common reference height of 6,721.2 km from the center of the Earth (~350 km above ground; around the nomial F-region peak height) unless otherwise stated.

## 3. Results

The blob event of interest occurred near the northeastern coast of South America around 23:40 UT on 21 January 2021. The date was extremely quiet with the daily minimum Dst index of −5 nT. Figure 1 shows line plots of in situ plasma parameters sampled along the ICON trajectory. The top two panels present plasma density (a) in its original reading, and (b) after high-pass filtering (by removing a background defined by a Savitzky-Golay filter of order 2 having a window size of 31 s) and rectification (i.e., taking absolute values of the remnant bipolar fluctuations). The filtered/rectified signals represent small-scale irregularities (e.g., Stolle et al., 2006; Xiong et al., 2010), such as EPBs and blobs that will be the focus of this study. In Figure 1b, the black horizontal dashed line represents an event threshold for plasma irregularity identification, and the small black rectangles at the level of 0.05 denote positive detection of an event by the method of Park et al. (2021). Figure 1c presents the fraction of oxygen ions to the total ion density. In Figure 1d, the green solid line is the ground track of ICON in the GLAT-GLON space. The blue dashed slant line marks the location of the dip equator at 600 km altitude, and the gray contours with numbers represent the solar zenith angle (SZA), calculated by the information at https://en.wikipedia.org/wiki/Solar_zenith_angle. Figures 1e–1g provide the three components of ion velocity: (e) outward velocity toward outer L-shells and perpendicular to B-field (i.e., upward at the dip equator), (f) eastward velocity in the direction perpendicular to B-field, and (g) parallel velocity completing the triads and along the B-field (positive northward). The bottom panel shows ion temperature measured by the ICON/IVM. The region of interest is shaded yellow.

The event in Figure 1 is a typical low-latitude blob exhibiting nearly all the relevant properties reported before. The scale size (Figure 1a) is about 500 km (~5° in GLON), which is similar to that of Kil et al. (2019, Figure 2) and Wang et al. (2019, Figure 1b). The blob contains fine substructures (Figure 1b) so as to be detected by the automatic identification method of Park et al. (2021) that can detect irregularities of scale sizes between ~15 and ~230 km. That is, though the blob in Figure 1a appears wider than 230 km (~2° in GLON), it contains small-scale fluctuations (Figure 1b) whose scale sizes are smaller than the 230 km. Existence of these substructures allows the method of Park et al. (2021) to identify the blob automatically (small black squares in Figure 1b). The high-pass-filtered/rectified plasma density clearly shows that only the blob region exhibits enhanced fluctuations. In Figure 1c, the oxygen ion fraction of the blob is higher than in the ambient plasma, which conforms to Kil et al. (2011). Figures 1e and 1f show that the E × B drift velocity inside the blob is more outward and eastward than the ambient values while the drift peak locations are zonally (westward) offset from that of the ion density peak. This feature is in good agreement with Klenzing et al. (2011). Field-aligned flow velocity in Figure 1g is similar to the ambient values; it is only weakly depressed from the background. Note that Klenzing et al. (2011, Figure 3) reported that either poleward or equatorward ion flow deflection can accompany blobs. The

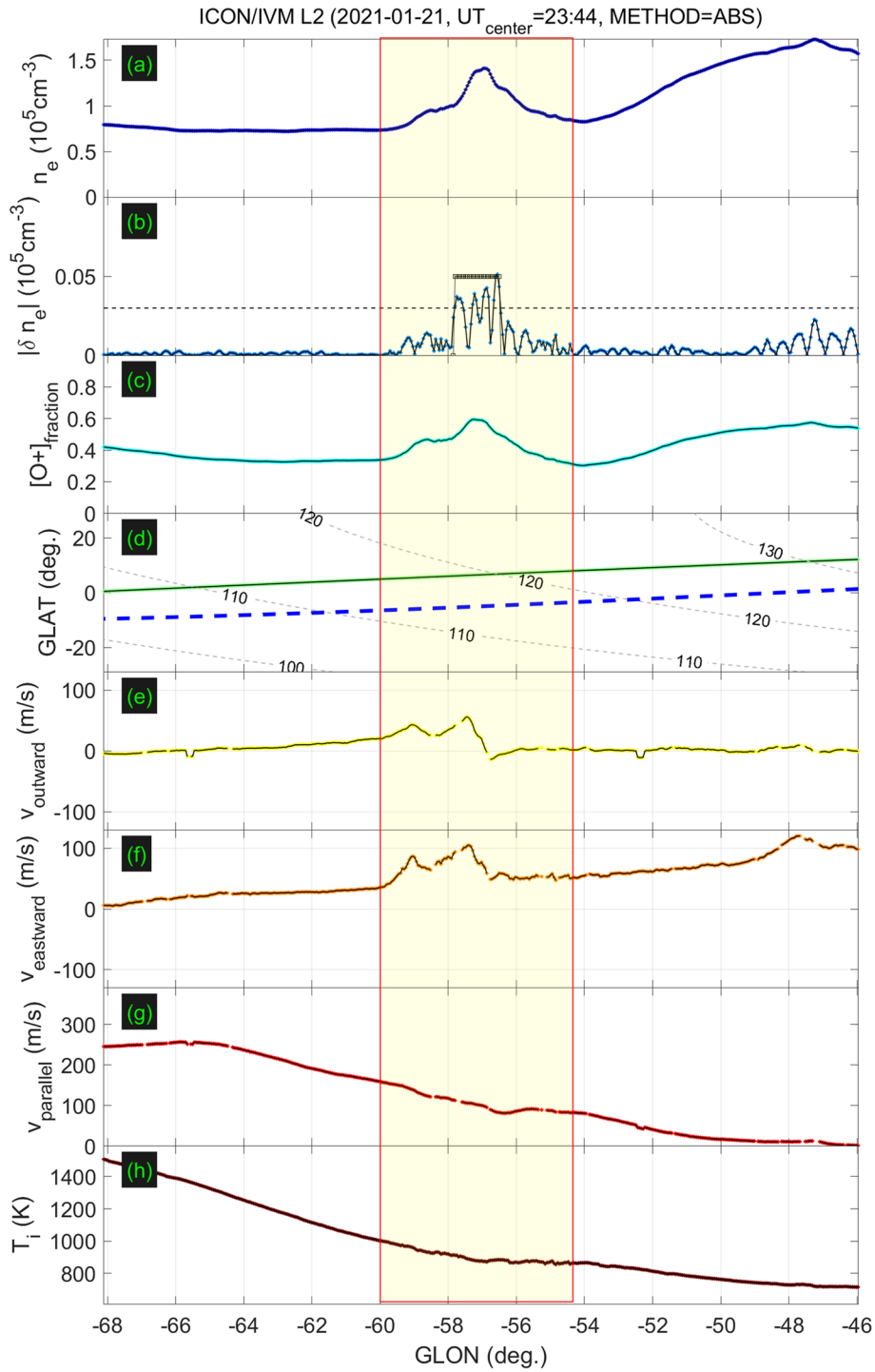


**Figure 1.** ICON/IVM data on 21 January 2021: (a) in situ plasma density, (b) high-pass-filtered and rectified plasma density for automatic irregularity identification, (c) oxygen ion fraction, (d) spacecraft ground track in the geographic coordinates, (e) ion velocity toward higher L-shells, (f) ion velocity toward magnetic east, (g) ion velocity parallel to B-field lines, and (h) ion temperature. In panel (b), the horizontal black dashed line represents event detection threshold while the small black squares signal an event identified automatically. In panel (d), the slant blue dashed line corresponds to the dip equator while the gray contours with numbers correspond to solar zenith angle.

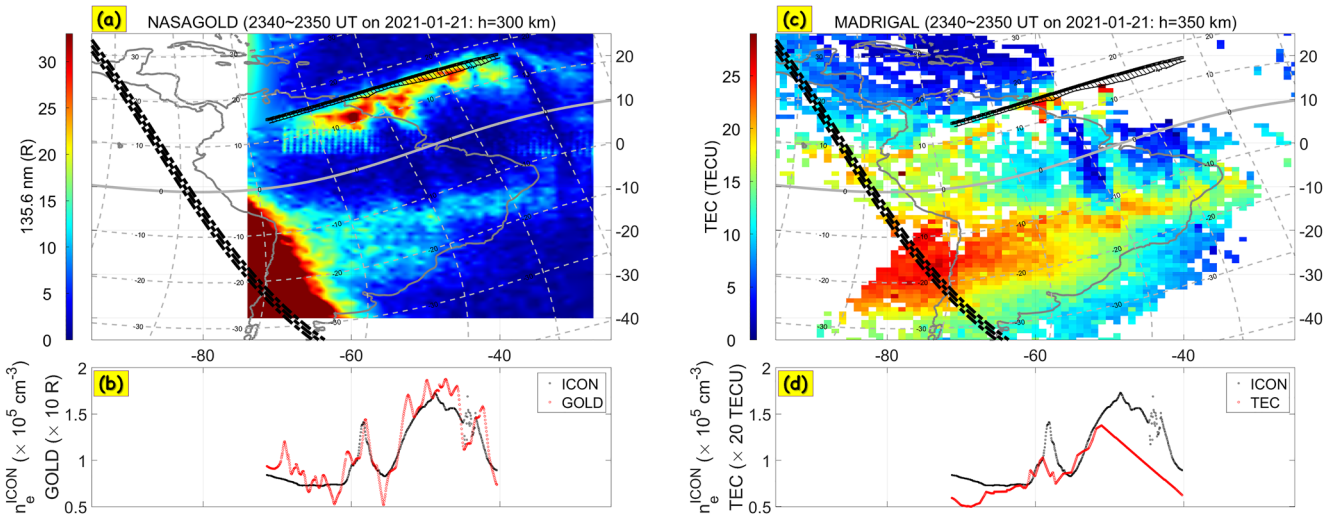


**Figure 2.** (a) 135.6 nm nightglow intensity obtained from the Global-scale Observations of the Limb and Disk (GOLD) nightside disk data, (b) plasma density and 135.6 nm nightglow intensity profiles resampled along the Ionospheric Connection Explorer (ICON) trajectory mapped along the field line down to 300 km, (c) global total electron content (TEC) map, and (d) plasma density and TEC profiles resampled along the mapped ICON trajectory down to 350 km. MLAT-MLON grid lines are given as gray dashed curves. The thickest black rope is the solar zenith angle of 90°. The thick black lines in panels (a and c) denote the mapped ICON trajectory while the hatched thin black curves represent relative variations of ICON/IVM plasma density.

field-aligned velocity variations are not zonally offset from the plasma density variations, which is also consistent with Klenzing et al. (2011). The blob ion temperature in Figure 1h does not exhibit a clear trend around the blob. This feature may be different from the examples in Park et al. (2003). However, many of the previous articles about blobs did not consider the temperature variations as a key ingredient of blob identification (e.g., Choi et al., 2012). Hence, the event in Figure 1 can be deemed a representative low-latitude blob.

Fortunately, the ICON event occurred within the GOLD FOV, which can put the former data into a wider two-dimensional context. In Figure 2a, the color palette represents the intensity of 135.6 nm FUV nightglow (integrated over 133 ~ 137 nm), which reflects the ionospheric electron content. The GOLD data are mapped onto the regular Cartesian GLAT-GLON grids (0.15° × 0.15°) using the MATLAB function, "*griddata*." The gray dashed curves correspond to grid lines of MLAT and MLON (at intervals of 10° each), and the thick gray solid curve represents the dip equator. The thickest black rope signifies SZA of 90°, that is, approximate location of the sunset terminator. The thick black solid line in the northern hemisphere is the ICON trajectory which is mapped along the magnetic field from the ICON height (i.e., geocentric distances of 6,371.2 km plus ICON altitude readings) to the standard GOLD reference altitude of 300 km (i.e., geocentric distances of 6,671.2 km). For the field-aligned mapping, the CHAOS magnetic field model is used (e.g., Finlay et al., 2016, 2020). Black hatches along the ICON trajectory represent relative variations of plasma density measured by ICON/IVM. In Figure 2a, we can see that the ICON blob event in Figure 1 is collocated with a region of enhanced 135.6 nm nightglow in the GOLD image. This coincidence is more conspicuous in Figure 2b, which directly compares the ICON/IVM plasma density (black) with the GOLD 135.6 nm intensity resampled along the mapped ICON trajectory (red) using the *griddata* function. The agreement between the two lines in Figure 2b confirms that ICON and GOLD observed the same phenomenon.

Figures 2c and 2d are similar to Figures 2a and 2b, but with a Madrigal TEC map instead of the GOLD 135.6 nm images. Note that the white areas do not represent low-TEC regions, but data gaps. The ICON trajectory (thick black curve) in Figure 2c is mapped along the field line down to 350 km, the standard reference height of the Madrigal TEC data, which is 50 km higher than that of the GOLD data. In Figure 2d, the agreement is good between ICON/IVM and TEC resampled along the mapped ICON trajectory, which supports the GOLD observations. Besides the enhancement in the ICON ion density, which corresponds to the GOLD 135.6 nm intensity and TEC increase at about −58° GLON, a second enhancement exists and peaks at about −48° GLON. This second, broader peak may also represent a blob and will be further discussed later.

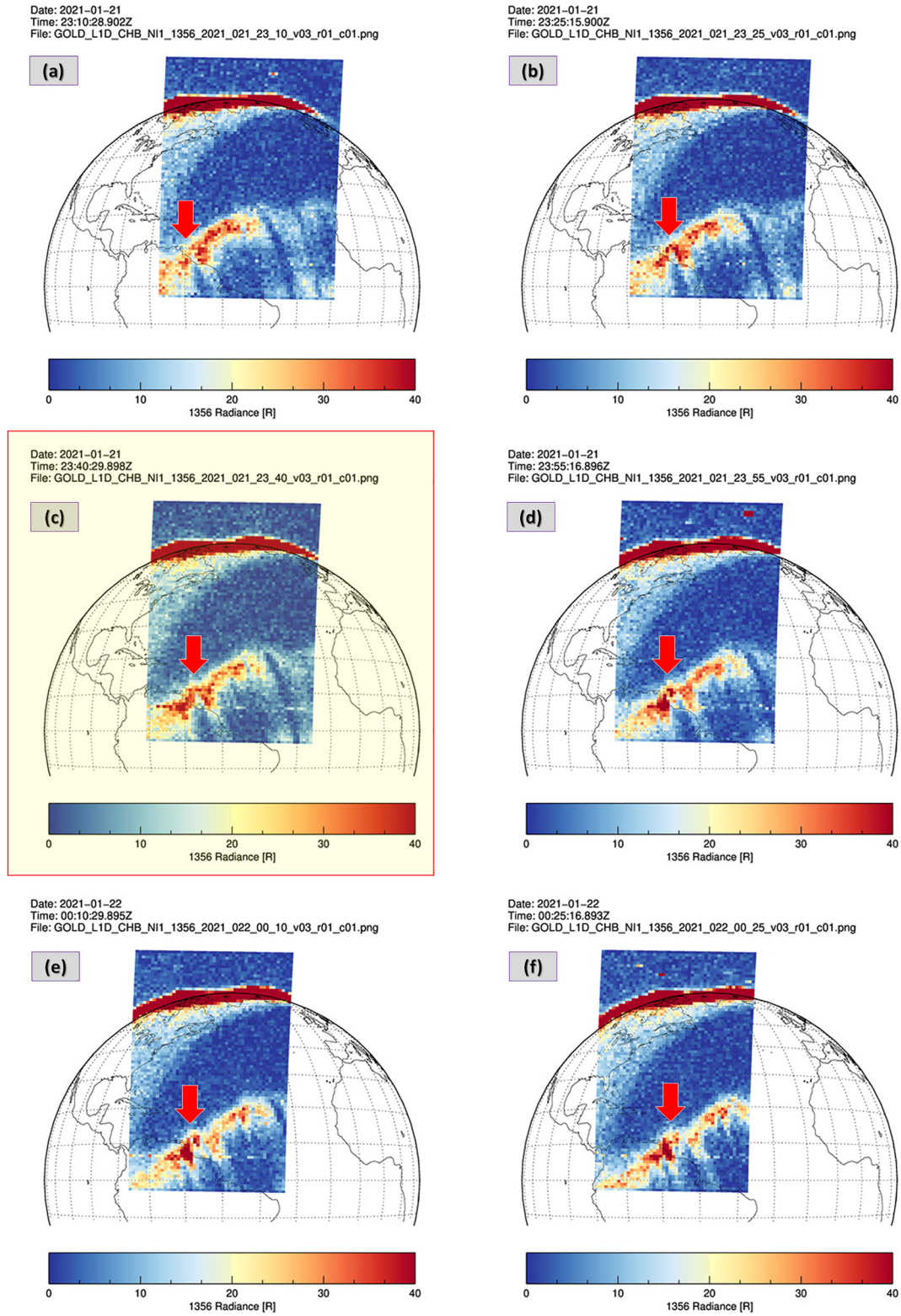


**Figure 3.** Time series of the Global-scale Observations of the Limb and Disk (GOLD) Channel-B 135.6 nm nightglow images. The image corresponding to the Ionospheric Connection Explorer (ICON) blob event (panel (c)) is highlighted with yellow shades. The red arrow in each panel points to the approximate location of the ICON blob.

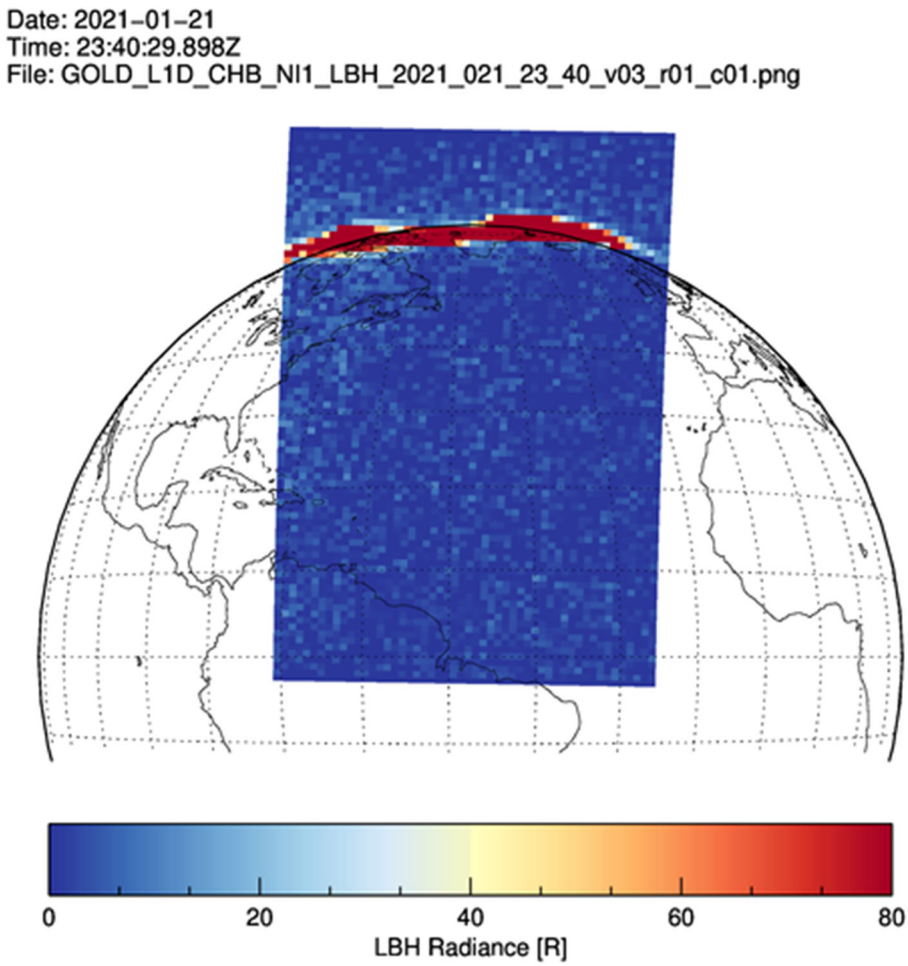


**Figure 4.** Global-scale Observations of the Limb and Disk (GOLD) Channel-B Lyman-Birge-Hopfield (LBH) nightglow image corresponding to Figure 2a. No conspicuous blob signature can be identified in the figure.

Figure 3 is a time series of the GOLD 135.6 nm images: panel *c* (shaded yellow) corresponds to the ICON blob in Figure 1. Red arrows point to approximate locations of the blob event shown in Figure 2. In Figure 3, we confirm that the ICON blob (see the red arrows) is located at the poleward edge of an EPB, has an inverted-V shape, and looks like the "*latitudinal displacements of the equatorial ionization anomaly*" reported by Eastes et al. (2019, Figure 4). From Figures 3a–3c, the 135.6 nm nightglow at the EPB poleward edge gradually intensifies. Later, the enhancement breaks down into substructures as can be seen from Figures 3d–3f. The local enhancement of 135.6 nm nightglow lasted at least for 1 hr between 23:25 (Figure 3b) and 00:25 next day (Figure 3f). The blob structures (or intensified poleward edge of the EPB) cannot be seen in the $N_2$ Lyman-Birge-Hopfield (LBH) bands in the GOLD data, as shown in Figure 4 (see also https://gold.cs.ucf.edu/data/search/). The absence of LBH emissions supports that the 135.6 nm nightglow enhancement is not related to energetic particle precipitations.

Figure 5 is similar to Figure 3, but with the GOLD 135.6 nm nightglow replaced by the Madrigal TEC between 22:30 and 24:00 UT. The highlighted panel (Figure 5e) corresponds to the time of the ICON blob in Figure 1. The TEC maps generally support the GOLD images in that the ICON blob event corresponds to an enhanced TEC region which sits on the EPB poleward edge and gradually intensifies with time.

Besides the EPB and related blob discussed above, more EPBs and blobs can be identified in the ICON, GOLD, and TEC data. In Figure 1, another enhancement exists in the electron density (Figure 1a) and eastward drift velocity (Figure 1f) at about −48° GLON, which accompanies an increase, although weaker, in the oxygen ion fraction (Figure 1c) and outward drift (Figure 1e). In Figure 2, two enhancements in 135.6 nm nightglow along the ICON track occur at higher latitudes around −58° and −48° GLON (Figure 2a), and similar enhancements in

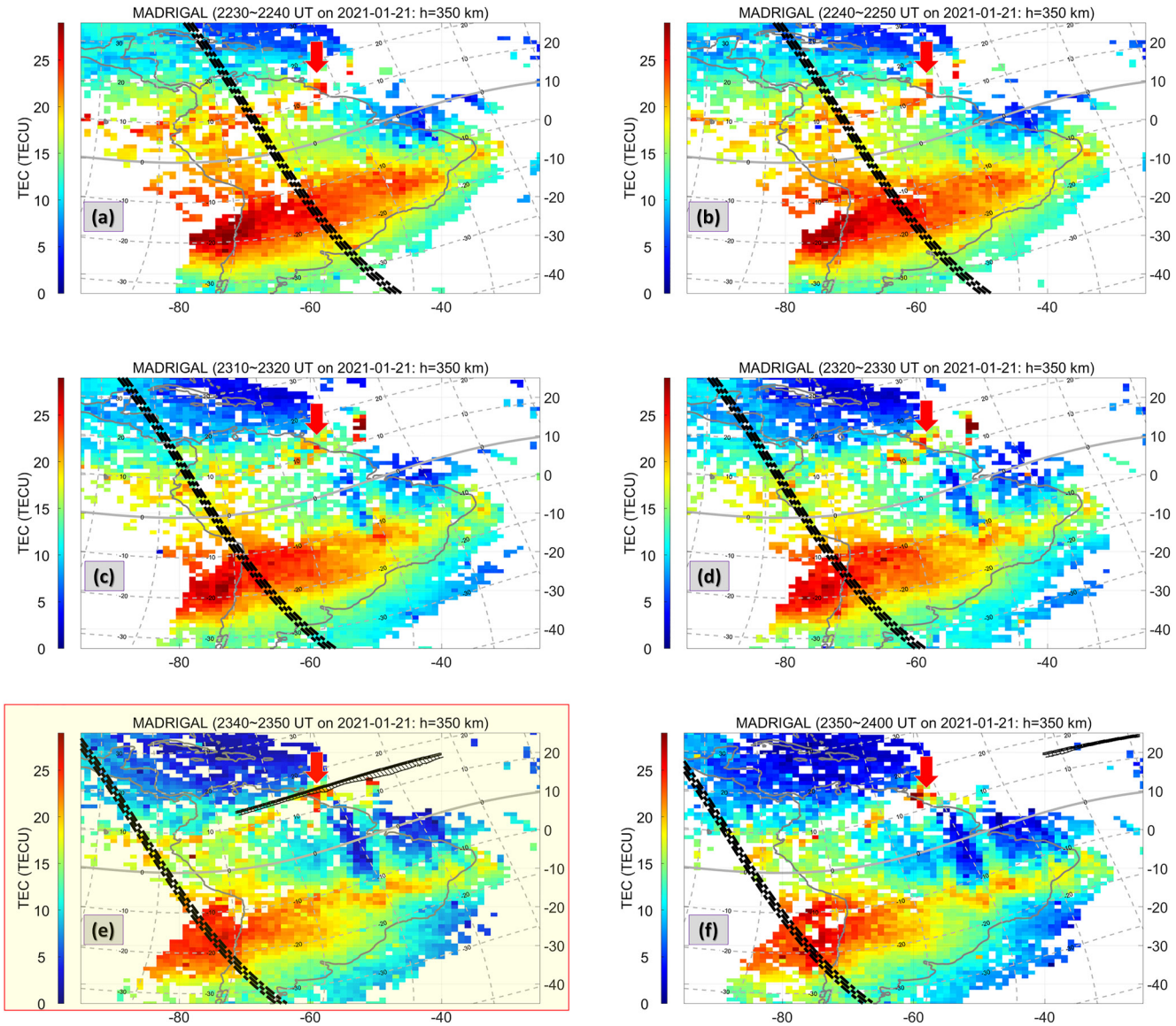


**Figure 5.** Similar to Figure 3, but presenting total electron content (TEC) between 22:30 UT and 24:00 UT instead of the Global-scale Observations of the Limb and Disk (GOLD) 135.6 nm nightglow.

TEC occur at the same longitudes (Figure 2c). The two well separated enhancements can be seen more clearly in Figures 2b and 2d. The first peak around −58° GLON is the blob discussed above, and the second and wider peak near −48° GLON may represent another blob. Furthermore, each TEC enhancement sits at the poleward edge of a depleted TEC band (an EPB). The quasi-periodic distribution of the EPBs and corresponding ion density/TEC enhancements (blobs) are also obvious in Figure 5. A third decrease in equatorial TEC starts to occur in Figure 5e, and the center of the TEC decrease is approximately located at −60° GLON over the magnetic equator. This TEC decrease deepens in Figure 5f and evolves into an EPB while an enhancement in TEC occurs at the poleward edge of this third EPB. The three EPBs and related blobs all move eastward.

Time series of the GOLD 135.6 nm (Movie S1) and TEC (Movie S2) images at the same 10 min cadence are available in Supporting Information S1. ICON orbits before and after the event in Figure 2 are also shown in the Movies. The ICON observations in the Movies exhibit good qualitative agreement with both TEC and GOLD data resampled along the ICON trajectory. Just, ICON-GOLD consistency (Movie S1) may be compromised near the border of GOLD images. So is ICON-TEC agreement (Movie S2) near large data gaps (e.g., above oceans). However, all these limitations of the movie images are not critical to our main conclusions. Note again that the

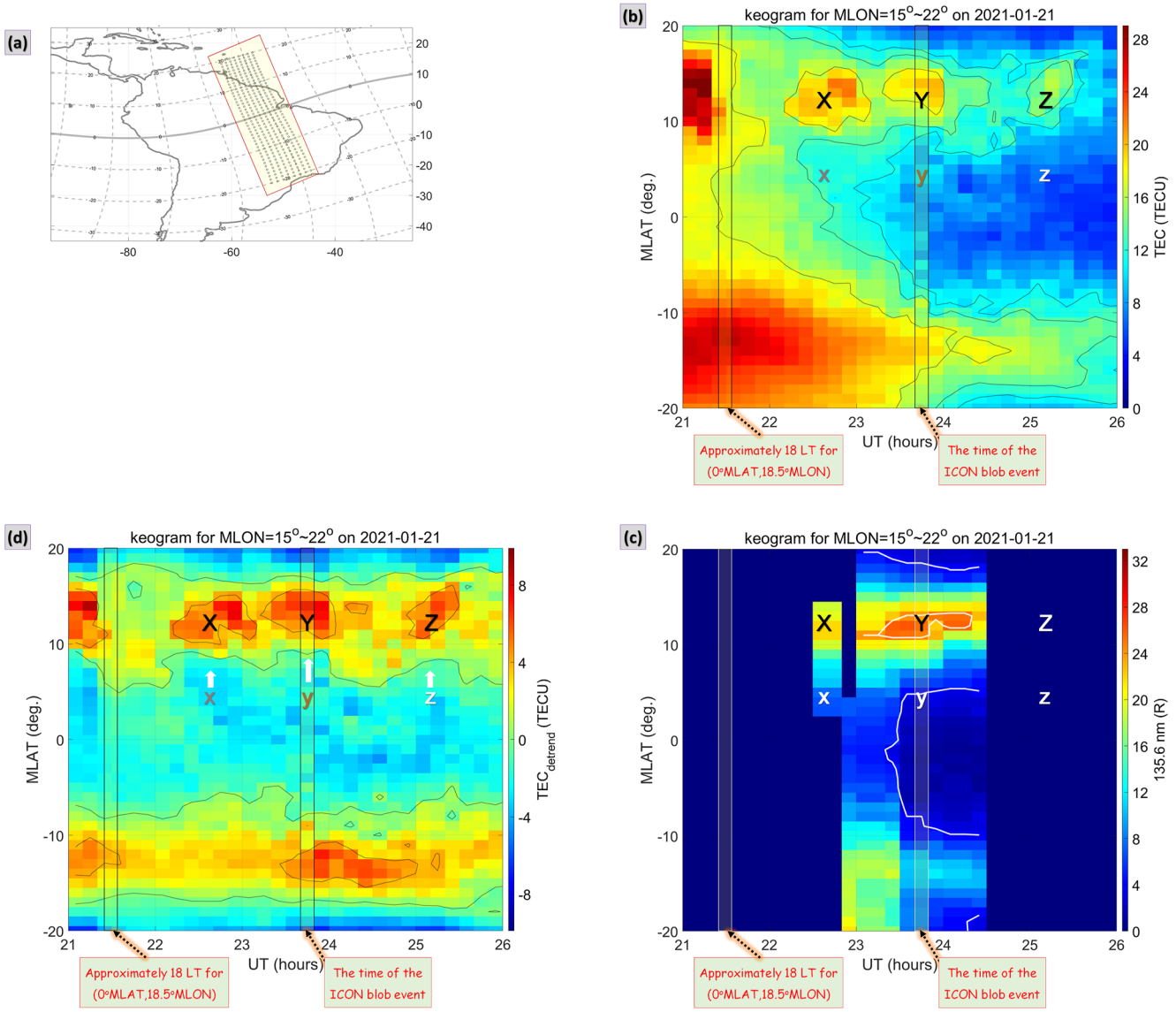


**Figure 6.** Clockwise from the top-left, (a) grid points used for constructing a keogram, (b) the resultant total electron content (TEC) keogram as a function of magnetic latitude (MLAT) and Universal Time (UT), and (c) the Global-scale Observations of the Limb and Disk (GOLD) 135.6 nm keogram. Blob-like TEC or 135.6 nm nightglow enhancements are marked with capital letters (*X*, *Y*, and *Z*) in panels (b–d) while the corresponding TEC or 135.6 nm nightglow depletions at equatorial regions are annotated with small letters (*x*, *y*, and *z*). Approximate times of the local sunset and the Ionospheric Connection Explorer (ICON) blob are marked with rectangles. Panel (d) is similar to panel (b), but showing detrended TEC which can emphasize the localized enhancements.

ICON trajectories are mapped along the geomagnetic field lines down to the nominal TEC (350 km) or 135.6 nm (300 km) image heights. As a result, the orbits in the Movies appear to bifurcate latitudinally when they cross the equator, and the mapped orbits in opposite hemispheres may zonally overlap due to nonzero declination angles.

We construct a keogram around the blob location to focus on the temporal evolution of the blob. First, we set up 2-dimensional grid points between +15° and +22° MLON and between −20° and +20° MLAT at 1° intervals: see the small black circles in Figure 6a. At those grid points, Madrigal TEC and GOLD 135.6 nm nightglow are resampled with the *griddata* function. For every 10 min and for every 1° MLAT interval, we estimate zonal median TEC values from all the eight grid points between +15° and +22° MLON. This procedure leads to a TEC keogram as shown in Figure 6b, which spans a time interval longer than shown in Figure 5. Contour lines are given to guide the readers' eyes. The region around the ICON blob at 23:40–23:50 UT is denoted with a capital letter, "*Y*." The TEC depletions (blue color) equatorward of "*Y*" are deemed EPBs and marked with a small letter,

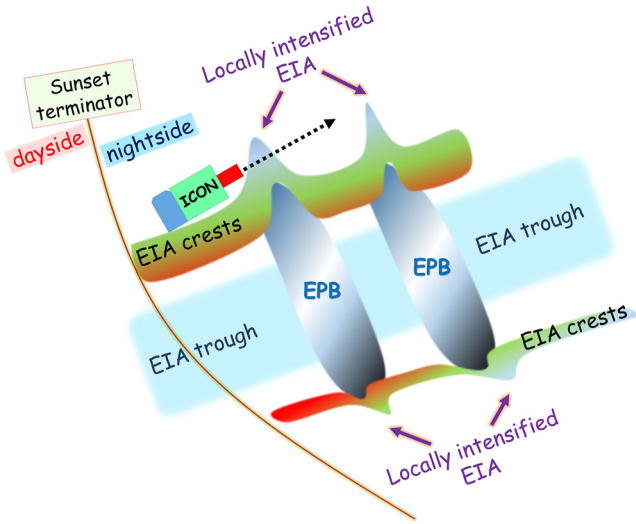


**Figure 7.** A pictorial summary of the blob event investigated in this article.

"*y*." In Figure 6b, the following points are worth mentioning. First, the ICON blob at 23:45 UT (*Y*) coincides with the local maximum in poleward extension of the EPB (*y*), reminding us of the EPB-related EIA extension reported by Eastes et al. (2019, Figure 4). Second, the ICON blob (*Y*) is not a monotonically decaying near-sunset EIA structure: the TEC enhancement in the keogram is isolated in UT (or equivalently, LT of the keogram region). This feature is also seen in the series of GOLD images (Figure 3), where the ICON blob region hosts stronger 135.6 nm nightglow than it was near the sunset. Third, the ICON blob (*Y*) does not exhibit MSTID-like equatorward motion (e.g., Shiokawa et al., 2003), as we can expect from the low MLAT (~15°) of the event: MSTIDs generally belong to mid-latitudes. Fourth, the temporal variations of the blob as shown in the keogram do not strictly exhibit hemispheric (north-south) conjugacy, which is also different than the generic MSTID property of hemispheric symmetry in the nightglow images and their keograms (e.g., Otsuka et al., 2004; Shiokawa et al., 2005, Figure 7).

Figure 6c is a keogram made out of the GOLD 135.6 nm nightglow. Due to the normal operation sequence of GOLD, the temporal coverage of Figure 6c is much smaller than in Figure 6b: the dark blue areas correspond to data gaps. Also, it is natural that the agreement between TEC (Figure 6b) and 135.6 nightglow data (Figure 6c) is imperfect because the former is a Line-of-sight integral of electron density while the latter is that of the "squared" density (Kil et al., 2013). Mathematically, the latter is more representative of the F-region peak region than the former. Despite the limitations, at least around the region of the ICON blob (denoted as "*Y*"), the GOLD keogram in Figure 6c supports the four conclusions drawn from Figure 6b. The "*Y*" region in the GOLD keogram features a local enhancement poleward of nightglow depletion (small "*y*"), and does not exhibit ordered equatorward movement or hemispheric conjugacy.

In Figure 6b, similar EPB-blob coincidence, albeit weaker, can be seen for the blob-like signatures before and after the ICON blob (*Y*-*y*); see the *X*-*x* and *Z*-*z* pairs in Figure 6. For the three pairs, deeper EPBs are not necessarily conjugate to stronger blobs. This is partly due to the natural decay of background TEC with LT. Consequently, blobs at a later UT (and LT of the keogram region) are weaker than at an earlier UT in absolute TEC levels while EPBs at the later UT are deeper (i.e., stronger). As a result, deeper EPBs apparently seem to be conjugate to weaker blobs.

To alleviate the effects of natural ionospheric decay with MLT, to each column in Figure 6b (i.e., to each MLT column) we apply a third-order detrend function and extract the residuals, which are shown in Figure 6d. This procedure largely removes the MLT-dependent background from Figure 6b. In Figure 6d, the local enhancements of EIA crests (*X, Y,* and *Z*) are more clearly seen, as well as their overall correspondence with nearby EPB intensity (*x, y*, and *z*: see the white arrows that mark TEC depletion contours expanding poleward), than in Figure 6b.

## 4. Discussion

### 4.1. Possible Generation Mechanisms for This Blob Event

The ICON blob event presented in Section 3, as may be expected from the low MLAT (~15°), lacks the following properties that are commonly expected for MSTIDs: (a) clear equatorward movement of the structure (Shiokawa et al., 2003), (b) source signatures propagating from mid-latitude regions (Shiokawa et al., 2003), (c) multiple wavefronts aligned in the northwest-southeast direction (Kil et al., 2019; Shiokawa et al., 2003), and (d) strict hemispheric symmetry in the temporal evolution of the plasma inhomogeneity (Kil et al., 2019; Otsuka et al., 2004; Shiokawa et al., 2005). We also checked other data sources to address possible existence of MSTIDs around the ICON blob event or its conjugate point. Detrended TEC maps provided by Nagoya University (https://stdb2.isee.nagoya-u.ac.jp/GPS/GPS-TEC/GLOBAL/MAP/index.html) do not exhibit conspicuous MSTIDs in South America (figures not shown). Also, from 630.0 nm nightglow images obtained by Boston University at Arecibo and Mercedes, which are located near the ICON blob event and its conjugate regions (http://sirius.bu.edu/dataview/), we could not find clear evidence of MSTIDs (figures not shown).

Rather, it seems more natural to connect the ICON blob event to EPBs because of (a) the two phenomena forming a latitudinal continuum sharing similar MLONs (Figures 2 and 3), (b) similar temporal variations of the blob and EPB (i.e., blob intensification in phase with EPB expansion; Figure 6), and (c) morphological similarity (inverted-V) between the EPB poleward part and the blob (Figures 2 and 3). In Introduction, we mentioned that, besides blob generation by MSTIDs, two different mechanisms had been suggested for blob generation by EPBs: E-field mapping (e.g., Le et al., 2003) and localized super-fountain (e.g., Huang et al., 2014; Krall et al., 2010). As will be discussed below, the ICON blob conforms to both mechanisms, and we cannot decisively tell which EPB-related mechanism is more plausible.

First, the ICON blob can be explained by the E-field mapping mechanism of Le et al. (2003), who suggested that enhanced eastward E-field inside EPBs can be mapped along B-field lines to the EIA crest region to generate blobs. In Figure 1e, outward drift (or eastward E-field) inside the blob is stronger than in the ambient, which agrees with Le et al. (2003). The additional zonal offset between the outward drift peak and the plasma density maximum may be explained by the fact that the locally enhanced outward drift is accompanied with eastward drift peaks (Figures 1e and 1f). That is, when high-density plasma below ICON is transported upward, the parcel is also displaced eastward. According to the mechanism of Le et al. (2003), the field-aligned plasma flows need not be more poleward than the ambient, just as seen in Figure 1g.

The second mechanism invoking super-fountain inside EPBs (Krall et al., 2010), which transports plasma toward poleward edges of an EPB flux tube and generates blobs there, can also explain the ICON blob. One might ask whether this mechanism is at odds with Figure 1g, where poleward velocity inside the blob is no higher than in the ambient plasma. According to Krall et al. (2010, Figure 7), however, the blob crest is not necessarily co-located with the parallel velocity peak, and parallel velocity near the poleward edge of the blob is no higher than in the ambient. These features agree with our ICON event, where the satellite skimmed the "poleward edge" of the GOLD blob (Figure 2). In addition, we might also argue that ion parallel flow around a mature blob is significantly affected by its own pressure gradient: see Klenzing et al. (2011, Figure 8). This effect can force the parallel flow to depend on the satellite location with respect to the substructures within the blob. Hence, blob encounter by a satellite needs not always accompany local enhancement of poleward field-aligned velocity, which might be the case of the ICON observation in Figure 1.

### 4.2. Previous Studies Including Similar Results

Figure 7 gives a pictorial summary of the blob event investigated in this article. ICON encountered a typical low-latitude blob on the nightside, and it was conjugate to the locally intensified (in both plasma density and magnetic latitudes) EIA crests in TEC and GOLD 135.6 nm images. The intensified EIA crests are wrapped around EPBs located at similar magnetic longitudes, which implies physical connections between the two. The northern and southern crests are not always symmetric, possibly due to inter-hemispheric wind (e.g., Krall et al., 2009, Figure 4) that prevails during solstice seasons. Hence, some blobs may appear hemispherically conjugate while others may not.

We expect that not all EPBs lead to the configuration in Figure 7: it depends on latitudinal extents of EPBs with respect to the EIA crests. There can be three possible relationships between EPBs and EIA crests. First, the poleward edges of an EPB may not reach the EIA crests, so that there is no obvious variation of the crests associated with the EPB. Second, when the poleward edges of an EPB reach the EIA crests, the outward $E \times B$ drifts and the fountain effects cause formation of plasma density enhancements at the crests. This is the situation we analyze in this study and depict in Figure 7. Third, EPBs can cross through the EIA crests and reach higher latitudes. In such cases, latitudinally continuous depletions are seen from the equator to poleward of the EIA crests. Then, the remnant EIA crests may look patchy, but would be zonally sandwiched between EPBs, which is different from our event.

In retrospect, structures similar to that in Figure 7 can be found in a number of previous studies. First of all, GOLD 135.6 nm nightglow images in Cai et al. (2021, Figures 2–4), Eastes et al. (2019, Figures 2–4), and Karan et al. (2020, Figures 1–2) presented such structures, that is, locally intensified EIA crests at the border of EPBs. As for 630.0 nm nightglow, Wu et al. (2018, Figures 2 and 3) reported "*edge plasma enhancement*" at EPB boundaries. Fine-scale computer simulations also presented plasma density enhancement surrounding EPBs, for example, Huba and Liu (2020, Figure 5), Yokoyama et al. (2015, Figures 2 and 3), and Yokoyama et al. (2019,

Figure 3). Just, none of the previous studies explicitly addressed the possibility that the local EIA intensification can appear as a blob when sampled by an LEO satellite. In Supporting Information S1, Movies S3–S6 are similar to Movies 1–2, but for the previous (Movies S3 and S4) and following days (Movies S5 and S6). The Movies also show local intensification of EIA crests at EPB boundaries, implying that such phenomena are quite common.

Therefore, if local intensification of EIA crests at EPB boundaries can make blob-like signatures in LEO plasma data under favorable observation geometry (as was shown in this article), common occurrence of the EIA intensification (as was shown by previous articles mentioned above and by the Movies in Supporting Information S1) suggests that they can be a significant contributor to low-latitude blob generation. More event studies with different satellites would be highly warranted in this respect.

## 5. Summary and Conclusion

On 21 January 2021, ICON encountered a typical low-latitude blob around the northeastern part of South America. The region was slightly poleward of the northern EIA peak and before local midnight. The geomagnetic activity was extremely low. With the help of two-dimensional images of 135.6 nm nightglow and TEC, which give a continental-scale (>2,000 km) context to the ICON blob event, we have found the following features of the blob.

1. The ICON blob was colocated with the enhanced 135.6 nm nightglow and TEC at the poleward edge of an EPB. Existence of such spatial structures in GOLD images was previously reported by Eastes et al. (2019, Figure 4), but not explicitly related to blobs in that article
2. A time series of GOLD images demonstrate that the ICON blob originated from enhanced plasma content on the EPB poleward edge, which gradually intensified with substructures. According to the GOLD image sequence, the blob lifetime was at least 1 hr
3. The GOLD LBH band images do not exhibit the blob signature, which implies absence of energetic particle precipitations
4. Unlike typical MSTIDs, the blob in the 135.6 nm and TEC images neither had a fixed wavefront direction (e.g., from northwest to southeast) nor moved southwestward. Also, the blob did not exhibit strict hemispheric symmetry. Rather, the ICON blob event can be explained by the two mechanisms related with EPBs in the presence of inter-hemispheric wind, as suggested by Krall et al. (2010)

This study has its significance in the following respects.

1. This is the first definitive imaging of a low-latitude plasma blob. Temporally resolved FUV imaging is free from the plasma-neutral ambiguity of previous 630.0 nm imaging
2. This is the first imaging of a plasma blob using a multi-wavelength FUV instrument. As expected, the blob has no emission in the LBH bands. Although the result is within the range of expectation, this article gives an observational confirmation for the first time
3. This study gives the first seamless continental-scale (>2,000 km) images around plasma blobs, which put LEO in situ observations in a broader context

As there have been many reports on blob generation mechanisms, each with its own supporting evidence, it suggests that there exist two (or more) different kinds of blobs: ones related with EPBs (e.g., Huang et al., 2014; Le et al., 2003; Wang et al., 2019; Wu et al., 2018; Yokoyama et al., 2007) and those related with MSTIDs (e.g., Choi et al., 2012; Haaser et al., 2012; Kil et al., 2011, 2019). Our case study does not elucidate which mechanism is the dominant one in a statistical sense. For addressing the detailed evolution of various low-latitude blobs, further studies are warranted; especially for the upcoming solar maximum during which both EPB activity and ground-based TEC map resolution would be higher than now. Those observations can also elucidate whether the dominant mechanisms of blob generation differ for different solar/geomagnetic activities. Statistics of ion/electron temperature variations inside blobs may give additional constraints on the blob generation mechanisms. Deeper understanding of blobs can also benefit studies on natural electromagnetic waves in the ionosphere because blobs are known to affect the waves (H. Kim et al., 2020).

## Data Availability Statement

The ICON data are open to the public at: https://icon.ssl.berkeley.edu/Data. The GOLD data and QuickLook's are available at: https://gold.cs.ucf.edu/data/search/. The Madrigal TEC data and overview plots can be downloaded from http://cedar.openmadrigal.org/. The CHAOS magnetic field model is provided at: https://www.space.dtu.dk/english/research/scientific_data_and_models/magnetic_field_models.

**Acknowledgments**
The authors are grateful to C. Martinis for valuable discussions on the signatures of low-latitude plasma blobs in two-dimensional nightglow images. Extensive comments by R. A. Heelis on blob generation mechanisms are also acknowledged. J. Park was supported by the National Research Council of Science & Technology (NST) grant by the Korean government (MSIT; No. CPS21161-120). CSH at the Air Force Research Laboratory was supported by NASA grant NNH22OB17A.

## References

Cai, X., Burns, A. G., Wang, W., Qian, L., Liu, J., Solomon, S. C., et al. (2021). Observation of postsunset OI 135.6 nm radiance enhancement over South America by the GOLD mission. *Journal of Geophysical Research: Space Physics*, *126*, e2020JA028108. https://doi.org/10.1029/2020JA028108

Chen, Y., Ma, G., Huang, W., Shen, H., & Li, J. (2008). Night-time total electron content enhancements at equatorial anomaly region in China. *Advances in Space Research*, *41*(4), 617–623. https://doi.org/10.1016/j.asr.2007.07.035

Choi, H.-S., Kil, H., Kwak, Y.-S., Park, Y.-D., & Cho, K.-S. (2012). Comparison of the bubble and blob distributions during the solar minimum. *Journal of Geophysical Research*, *117*, A04314. https://doi.org/10.1029/2011JA017292

Eastes, R. W., McClintock, W. E., Burns, A. G., Anderson, D. N., Andersson, L., Aryal, S., et al. (2020). Initial observations by the GOLD mission. *Journal of Geophysical Research: Space Physics*, *125*, e2020JA027823. https://doi.org/10.1029/2020JA027823

Eastes, R. W., Solomon, S. C., Daniell, R. E., Anderson, D. N., Burns, A. G., England, S. L., et al. (2019). Global-scale observations of the equatorial ionization anomaly. *Geophysical Research Letters*, *46*, 9318–9326. https://doi.org/10.1029/2019GL084199

Finlay, C. C., Kloss, C., Olsen, N., Hammer, M. D., Tøffner-Clausen, L., Grayver, A., & Kuvshinov, A. (2020). The CHAOS-7 geomagnetic field model and observed changes in the South Atlantic Anomaly. *Earth, Planets, and Space*, *72*, 156. https://doi.org/10.1186/s40623-020-01252-9

Finlay, C. C., Olsen, N., Kotsiaros, S., Gillet, N., & Tøffner-Clausen, L. (2016). Recent geomagnetic secular variation from Swarm and ground observatories as estimated in the CHAOS-6 geomagnetic field model. *Earth, Planets, and Space*, *68*, 112. https://doi.org/10.1186/s40623-016-0486-1

Haaser, R. A., Earle, G. D., Heelis, R. A., Klenzing, J., Stoneback, R., Coley, W. R., & Burrell, A. G. (2012). Characteristics of low-latitude ionospheric depletions and enhancements during solar minimum. *Journal of Geophysical Research*, *117*, A10305. https://doi.org/10.1029/2012JA017814

Heelis, R. A., Stoneback, R. A., Perdue, M. D., Depew, M. D., Morgan, W. A., Mankey, M. W., et al. (2017). Ion velocity measurements for the Ionospheric Connections Explorer. *Space Science Reviews*, *212*(1–2), 615–629. https://doi.org/10.1007/s11214-017-0383-3

Huang, C.-S., Le, G., de La Beaujardière, O., Roddy, P. A., Hunton, D. E., Pfaff, R. F., & Hairston, M. R. (2014). Relationship between plasma bubbles and density enhancements: Observations and interpretation. *Journal of Geophysical Research: Space Physics*, *119*, 1325–1326. https://doi.org/10.1002/2013JA019579

Huba, J. D., & Liu, H.-L. (2020). Global modeling of equatorial spread F with SAMI3/WACCM-X. *Geophysical Research Letters*, *47*, e2020GL088258. https://doi.org/10.1029/2020GL088258

Immel, T. J., England, S. L., Mende, S. B., Heelis, R. A., Englert, C. R., Edelstein, J., et al. (2018). The Ionospheric Connection Explorer mission: Mission goals and design. *Space Science Reviews*, *214*, 13. https://doi.org/10.1007/s11214-017-0449-2

Karan, D. K., Daniell, R. E., England, S. L., Martinis, C. R., Eastes, R. W., Burns, A. G., & McClintock, W. E. (2020). First zonal drift velocity measurement of equatorial plasma bubbles (EPBs) from a geostationary orbit using GOLD data. *Journal of Geophysical Research: Space Physics*, *125*, e2020JA028173. https://doi.org/10.1029/2020JA028173

Kil, H., Choi, H.-S., Heelis, R. A., Paxton, L. J., Coley, W. R., & Miller, E. S. (2011). Onset conditions of bubbles and blobs: A case study on 2 March 2009. *Geophysical Research Letters*, *38*, L06101. https://doi.org/10.1029/2011GL046885

Kil, H., Lee, W. K., Shim, J., Paxton, L. J., & Zhang, Y. (2013). The effect of the 135.6 nm emission originated from the ionosphere on the TIMED/GUVI $O/N_2$ ratio. *Journal of Geophysical Research: Space Physics*, *118*, 859–865. https://doi.org/10.1029/2012JA018112

Kil, H., Paxton, L. J., Jee, G., & Nikoukar, R. (2019). Plasma blobs associated with medium-scale traveling ionospheric disturbances. *Geophysical Research Letters*, *46*, 3575–3581. https://doi.org/10.1029/2019GL082026

Kil, H., Su, S.-Y., Paxton, L. J., Wolven, B. C., Zhang, Y., Morrison, D., & Yeh, H. C. (2004). Coincident equatorial bubble detection by TIMED/GUVI and ROCSAT-1. *Geophysical Research Letters*, *31*, L03809. https://doi.org/10.1029/2003GL018696

Kim, H., Shiokawa, K., Park, J., Miyoshi, Y., Hwang, J., & Kadokura, A. (2020). Modulation of Pc1 wave ducting by equatorial plasma bubble. *Geophysical Research Letters*, *47*, e2020GL088054. https://doi.org/10.1029/2020GL088054

Kim, V. P., & Hegai, V. V. (2016). Low latitude plasma blobs: A review. *Journal of Astronomy and Space Sciences*, *33*(1), 13–19. https://doi.org/10.5140/JASS.2016.33.1.13

Klenzing, J. H., Rowland, D. E., Pfaff, R. F., Le, G., Freudenreich, H., Haaser, R. A., et al. (2011). Observations of low-latitude plasma density enhancements and their associated plasma drifts. *Journal of Geophysical Research*, *116*, A09324. https://doi.org/10.1029/2011JA016711

Krall, J., Huba, J. D., Joyce, G., & Yokoyama, T. (2010). Density enhancements associated with equatorial spread F. *Annales Geophysicae*, *28*, 327–337. https://doi.org/10.5194/angeo-28-327-2010

Krall, J., Huba, J. D., & Martinis, C. R. (2009). Three-dimensional modeling of equatorial spread F airglow enhancements. *Geophysical Research Letters*, *36*, L10103. https://doi.org/10.1029/2009GL038441

Laundal, K. M., & Richmond, A. D. (2017). Magnetic coordinate systems. *Space Science Reviews*, *206*, 27–59. https://doi.org/10.1007/s11214-016-0275-y

Le, G., Huang, C.-S., Pfaff, R. F., Su, S.-Y., Yeh, H.-C., Heelis, R. A., et al. (2003). Plasma density enhancements associated with equatorial spread F: ROCSAT-1 and DMSP observations. *Journal of Geophysical Research*, *108*(A8), 1318. https://doi.org/10.1029/2002JA009592

Makela, J. J., & Kelley, M. C. (2003). Using the 630.0 nm nightglow emission as a surrogate for the ionospheric Pedersen conductivity. *Journal of Geophysical Research*, *108*(A6), 1253. https://doi.org/10.1029/2003JA009894

Martinis, C., Baumgardner, J., Mendillo, M., Su, S.-Y., & Aponte, N. (2009). Brightening of 630.0 nm equatorial spread-F airglow depletions. *Journal of Geophysical Research*, *114*, A06318. https://doi.org/10.1029/2008JA013931

Otsuka, Y., Shiokawa, K., Ogawa, T., & Wilkinson, P. (2004). Geomagnetic conjugate observations of medium-scale traveling ionospheric disturbances at midlatitude using all-sky airglow imagers. *Geophysical Research Letters*, *31*, L15803. https://doi.org/10.1029/2004GL020262

Oya, H., Takahashi, T., & Watanabe, S. (1986). Observation of low-latitude ionosphere by the impedance probe onboard the Hinotori satellite. *Journal of Geomagnetism and Geoelectricity*, *38*, 111–123.

Park, J., Heelis, R., & Chao, C. K. (2021). Ion velocity and temperature variation around topside nighttime irregularities: Contrast between low- and mid-latitude regions. *Journal of Geophysical Research: Space Physics*, *126*, e2020JA028810. https://doi.org/10.1029/2020JA028810

Park, J., Lühr, H., Michaelis, I., Stolle, C., Rauberg, J., Buchert, S., et al. (2015). Westward tilt of low-latitude plasma blobs as observed by the Swarm constellation. *Journal of Geophysical Research: Space Physics*, *120*, 3187–3197. https://doi.org/10.1002/2014JA020965

Park, J., Min, K. W., Lee, J.-J., Kil, H., Kim, V. P., Kim, H.-J., et al. (2003). Plasma blob events observed by KOMPSAT-1 and DMSP F15 in the low-latitude nighttime upper ionosphere. *Geophysical Research Letters*, *30*(21), 2114. https://doi.org/10.1029/2003GL018249

Pimenta, A. A., Sahai, Y., Bittencourt, J. A., Abdu, M. A., Takahashi, H., & Taylor, M. J. (2004). Plasma blobs observed by ground-based optical and radio techniques in the Brazilian tropical sector. *Geophysical Research Letters*, *31*, L12810. https://doi.org/10.1029/2004GL020233

Rajesh, P. K., Liu, J. Y., Hsu, M. L., Lin, C. H., Oyama, K. I., & Paxton, L. J. (2011). Ionospheric electron content and NmF2 from nighttime OI 135.6 nm intensity. *Journal of Geophysical Research*, *116*, A02313. https://doi.org/10.1029/2010JA015686

Rideout, W., & Coster, A. (2006). Automated GPS processing for global total electron content data. *GPS Solutions*, *10*, 219–228. https://doi.org/10.1007/s10291-006-0029-5

Shiokawa, K., Ihara, C., Otsuka, Y., & Ogawa, T. (2003). Statistical study of nighttime medium-scale traveling ionospheric disturbances using midlatitude airglow images. *Journal of Geophysical Research*, *108*(A1), 1052. https://doi.org/10.1029/2002JA009491

Shiokawa, K., Otsuka, Y., Tsugawa, T., Ogawa, T., Saito, A., Ohshima, K., et al. (2005). Geomagnetic conjugate observation of nighttime medium-scale and large-scale traveling ionospheric disturbances: FRONT3 campaign. *Journal of Geophysical Research*, *110*, A05303. https://doi.org/10.1029/2004JA010845

Stolle, C., Lühr, H., Rother, M., & Balasis, G. (2006). Magnetic signatures of equatorial spread F as observed by the CHAMP satellite. *Journal of Geophysical Research*, *111*, A02304. https://doi.org/10.1029/2005JA011184

Vierinen, J., Coster, A. J., Rideout, W. C., Erickson, P. J., & Norberg, J. (2016). Statistical framework for estimating GNSS bias. *Atmospheric Measurement Techniques*, *9*, 1303–1312. https://doi.org/10.5194/amt-9-1303-2016

Wang, Z., Liu, H., Shi, J., Wang, G., & Wang, X. (2019). Plasma blobs concurrently observed with bubbles in the Asian-Oceanian sector during solar maximum. *Journal of Geophysical Research: Space Physics*, *124*. https://doi.org/10.1029/2018JA026373

Wang, Z., Shi, J. K., Torkar, K., Wang, G. J., & Wang, X. (2015). A case study on ionospheric scintillations at low-latitude associated with a plasma blob observed in situ. *Geophysical Research Letters*, *42*, 2109–2114. https://doi.org/10.1002/2015GL063493

Watanabe, S., & Oya, H. (1986). Occurrence characteristics of low-latitude ionospheric irregularities observed by impedance probe onboard Hinotori satellite. *Journal of Geomagnetism and Geoelectricity*, *38*, 125–149.

Wu, K., Xu, J., Xiong, C., & Yuan, W. (2018). Edge plasma enhancements of equatorial plasma depletions observed by all-sky imager and the C/NOFS satellite. *Journal of Geophysical Research: Space Physics*, *123*, 8835–8849. https://doi.org/10.1029/2018JA025809

Xiong, C., Park, J., Lühr, H., Stolle, C., & Ma, S. Y. (2010). Comparing plasma bubble occurrence rates at CHAMP and GRACE altitudes during high and low solar activity. *Annales Geophysicae*, *28*, 1647–1658. https://doi.org/10.5194/angeo-28-1647-2010

Yokoyama, T., Jin, H., & Shinagawa, H. (2015). West wall structuring of equatorial plasma bubbles simulated by three-dimensional HIRB model. *Journal of Geophysical Research: Space Physics*, *120*, 8810–8816. https://doi.org/10.1002/2015JA021799-T

Yokoyama, T., Jin, H., Shinagawa, H., & Liu, H. (2019). Seeding of equatorial plasma bubbles by vertical neutral wind. *Geophysical Research Letters*, *46*, 7088–7095. https://doi.org/10.1029/2019GL083629

Yokoyama, T., Su, S.-Y., & Fukao, S. (2007). Plasma blobs and irregularities concurrently observed by ROCSAT-1 and Equatorial Atmosphere Radar. *Journal of Geophysical Research*, *112*, A05311. https://doi.org/10.1029/2006JA012044